Journal of Solid State Chemistry 205 (2013) 91–96

Contents lists available at SciVerse ScienceDirect

Journal of Solid State Chemistry

journal homepage: www.elsevier.com/locate/jssc

Synthesis, characterization and magnetic behavior of Co/MCM-41 nano-composites

N. Cuello [a], V. Elías [a,c], M. Crivello [a], M. Oliva [b,d], G. Eimer [a,c,*]

[a] CITeQ-Universidad Tecnológica Nacional-Facultad Regional Córdoba, Maestro López esq. Cruz Roja Argentina, 5016 Córdoba, Argentina
[b] FaMAF-Universidad Nacional de Córdoba, Córdoba, Argentina
[c] CONICET, Argentina
[d] IFEG-CONICET, Argentina

ARTICLE INFO

Article history:
Received 26 April 2013
Received in revised form
26 June 2013
Accepted 28 June 2013
Available online 9 July 2013

Keywords:
MCM-41
Impregnation
Co species
Superparamagnetism
Metallic loading

ABSTRACT

Synthesis, structure and magnetic properties of Co/MCM-41 as magnetic nano-composites have been investigated. Mesoporous materials with different degrees of metal loading were prepared by wet impregnation and characterized by ICP, XRD, N_2 adsorption, UV–vis DRS, TPR and EPMA-EDS. Cobalt oxide clusters and Co_3O_4 nano-particles could be confined inside the mesopores of MCM-41, being this fact favored by the Co loading increasing. In addition, larger crystals of Co_3O_4 detectable by XRD also grow on the surface when the Co loading is enhanced. The magnetic characterization was performed in a SQUID magnetometer using a maximum magnetic applied field $\mu_0 Ha = 1$ T. While the samples with the higher Co loadings showed a behavior typically paramagnetic, a superparamagnetic contribution is more notorious for lower loadings, suggesting high Co species dispersion.

1. Introduction

The synthesis and study of the properties of magnetic systems with characteristic nano-dimensions has attracted the attention in recent years because of the continuous increase in the potential applications of new magnetic materials. It is known that nano-particles display properties that differ from their bulk counter-part giving rise to unique physical properties upon size reduction. The use of magnetic nano-sized particles can lead to revolutionary changes in many areas of high technology such as catalysis, biomedicine, ultra-high density magnetic storage media, high-frequency soft magnetic materials, electronics [1–9]. In particular, the biomedic applications include magnetic bioseparation, biological labeling and diagnostics, enhancement of contrast agents for magnetic resonance imaging, hyperthermia of tumors and drug-carrier design. The synthesis of magnetic nano-particles with a quite small size is extremely difficult because the individual particles tend to aggregate and/or coalesce. These problems can be overcome by fabricating magnetic nano-particles or clusters supported on porous solids. Thus, the production of heterogeneous magnetic materials with controlled composition and structure is a great challenge. Mesoporous materials, like MCM-41, have great advantages as supports due to the unique combination of high surface area, pore volume and ordered pore structure with narrow pore size distribution [10,11]. Thus, MCM-41 can be used as template to confine conveniently magnetic compounds in a quasi-one-dimensional array because of its particular topology of regular hexagonal parallel channels with usual average diameters of less than 5 nm. Therefore, these pore systems can act as nano-reactors, allowing the stabilization of metal high loadings to obtain nano-arrays of diverse metal species in its channels. In this context, the synthesis of mesoporous nano-composites having magnetic elements occluded in the nano-channels or inside the porous framework is very promising. In the biomedical field, these nano-composites offer high loading of drug/bioactive agents as well as the ability of selectively deliver the drug in the desired organs or tissues inside the body, by the application of an external magnetic field [12–16].

Many works describing the properties of magnetic mesoporous materials can be found in the literature [17–21]. Likewise, the synthesis and characterization of Co containing mesoporous molecular sieves for different applications have been extensively investigated [22–32]. However, their structural and magnetic properties as well as presence and location of different cobalt species varying with the metal loading degree continue under study. To our knowledge, until now Sato et al. have studied magnetic properties of Co^{II} mesoclusters dispersed in a mesoporous silicate, prepared by calcination of the MCM-41 molecular sieve soaked in $CoCl_2$ 0.01 M aqueous solution [33]; Haskouri et al.

* Corresponding author at: CITeQ-Universidad Tecnológica Nacional-Facultad Regional Córdoba, Maestro López esq. Cruz Roja Argentina, 5016 Córdoba, Argentina.
E-mail address: geimer@scdt.frc.utn.edu.ar (G. Eimer).

0022-4596/$ - see front matter © 2013 Elsevier Inc. All rights reserved.
http://dx.doi.org/10.1016/j.jssc.2013.06.028

have reported a magnetic study of silica-based MCM-41-like mesoporous materials with high cobalt content ($\infty \leq$ Si/Co$\leq$23) synthesized through a one-pot surfactant-assisted procedure from aqueous solution and using complexes (triethanolamine-like species) as ligands of the inorganic precursors [34]; Emamian et al. [35] have recently informed the magnetic characterization of a MCM-41 supported cobalt ferrite nano-composite; Morey et al. have presented a magnetic study of highly ordered Co-MCM-41 with 3 wt.% Co loading synthesized by using a direct procedure [36]; In this work we focus on nano-composites of cobalt species on MCM-41 prepared by a simple and fast post-synthesis method (wet impregnation). We discuss the influence of the Co content on the chemical and structural characteristics of the obtained materials and their connection to the magnetic properties.

2. Experimental

2.1. Synthesis

The metal-free MCM-41 mesoporous molecular sieve was synthesized as previously reported [37] following the method B, using cetyltrimethylammonium bromide (CTAB) (Merck 99%) as template and tetraethoxysilane (TEOS) (Aldrich 98%) as silicon source. The synthesis mixture (pH = 11.25) was stirred at room temperature for 4 h. Then, this gel was heated at 70 °C under stirring in a closed flask. The MCM-41 host, previously calcined for 5 h in oven at 500 °C, was modified with cobalt by the wet impregnation method. Different concentrations of an aqueous solution of the metal precursor ($Co(NO_3)_2 \cdot 6H_2O$, Riedel-de Haën 98%) were used to reach the desired loadings (0.060, 0.038, 0.018, 0.0087, 0.0034 M corresponding to 15, 10, 5, 2.5 and 1 wt.%, respectively). The MCM-41 host (0.75 g) was dispersed in 37.5 mL of the precursor solution at room temperature and then, the solvent (water) was slowly removed by rotary evaporation at 50 °C for 30 min. The resulting powder was dried at 60 °C and calcined for 9 h at 500 °C. The samples were designated as Co/*M*(*x*) where *M* indicates the MCM-41 mesoporous structure and *x* indicates the nominal percentage of metal loading.

2.2. Characterization

The X-ray diffraction patterns (XRD) were recorded in a Philips PW 3830 diffractometer with Cu*K*α radiation ($\lambda = 1.5418$ Å) in the range of 2θ from 1.5° to 7° and from 20° to 80°. A profile fitting was made to each maximum in the high angle range, and the mean crystallite size *D* of the corresponding phase was estimated using the Scherrer formulae: $D = 0.9\lambda/\beta \cos\theta$, where β (in radians) is the peak intrinsic breadth after subtraction of the instrumental contribution, λ is the X-ray wavelength and θ is the Bragg angle [38]. It is worth to note that the Scherrer equation was used in order to perform a rough estimation of the crystallite size. The specific surface, the pore size distribution, and the total pore volume were determined from N_2 adsorption–desorption isotherms obtained at −196 °C using a Micromeritics ASAP 2010. The surface was determined by the Brunauer–Emmet–Teller (BET) method in the pressure range of P/P_0: 0.01–0.21. The pore size distribution curves were determined by the Barret–Joyner–Halenda (BJH) method. UV–vis diffuse reflectance spectra (UV–vis DRS) in absorbance mode were recorded using a Jasco V 650 spectrometer with an integrating sphere in the wavelength range of 200–900 nm. The Co content was determined by inductively coupled plasma optical emission spectroscopy (ICP) using a VISTA-MPX CCD Simultaneous ICP-OES-VARIAN. The reducibility of the catalysts was measured by temperature-programmed reduction (TPR) experiments in a Quantachrome Chembet 3000. In these experiments, the samples were heated at a rate of 10 °C/min in the presence of H_2 (5% H_2/N_2 flow, 20 mL/min STP), and the reduction reaction was monitored by the H_2 consumption. The surface elemental Energy-dispersive X-ray analysis (EMPA-EDS) was conducted in an electron microprobe Jeol JXA 8230. The room temperature magnetization vs. field curves were measured in a Quantum Design SQUID magnetometer MPMS XL7 with static field up to $\mu_0 H = 1$ T. The hysteresis properties as the coercive field and remanent magnetic moment were estimated from the magnetization curves; they were well fitted by the sum of three contributions: a linear paramagnetic or diamagnetic contribution (LM), a ferromagnetic one (FM) [39], and a superparamagnetic-like one (SPM) [40], so that the total magnetization results: TM = LM+FM+SPM.

3. Results and discussion

The low-angle XRD patterns of all of the materials synthesized in this study are shown in Fig. 1. As it is observed, the XRD pattern of the MCM-41 sample exhibits three diffraction peaks assignable to the reflections (100), (110) and (200) typical of a mesoporous structure with hexagonal array of their uni-dimensional pores [41]. The high intensity and good resolution of XRD peaks indicate the long-range ordering and high quality of the synthesized material. All of the Co modified samples have a XRD pattern comparable to that of MCM-41 indicating that the mesoporous structure of the support is sustained after the impregnation and calcination process. Thus, this structure allowed a Co loading of up to ≈12 wt.% without collapsing. However, the XRD patterns appear less resolved and the intensity of the (100) diffraction peak is significantly decreased for the samples with higher Co loadings (between≈4 and 12 wt.%). This can be attributed to the nano-size

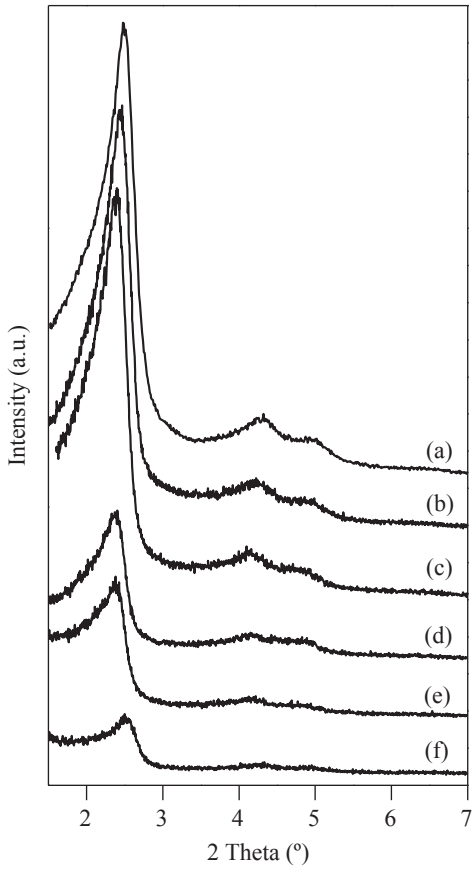

Fig. 1. Low-angle XRD patterns of samples: (a) MCM-41, (b) Co/M(1), (c) Co/M(2.5), (d) Co/M(5), (e) Co/M(10), (f) Co/M(15).

of impregnated Co species possibly confined inside the pores. Nevertheless, the regularity of the structure is certainly maintained despite the high Co loadings. Thus, our results are contrary to those reported by Khodakov et al. [25] who demonstrate that the mesoporous structure of MCM-41 is dramatically distorted on impregnation and drying and that no XRD peaks attributed to the hexagonal lattice have been found for the calcined Co/MCM-41 materials. The collapse of MCM-41 structure seems to be attributed to the hydrolysis of Si–O–Si bonds of the relatively thin amorphous silica walls. The pore wall thickness of MCM-41 materials corresponds to only a few SiO_4 groups and the easy reaction of these groups with water seems to be the reason why the hexagonally organized structure readily degrades during hydrolysis. We suggest that the higher stability of our materials, whose long-range ordering was not destroyed during aqueous impregnation, can be attributed to their wall thicknesses ($\sim$1 nm) larger than that of the typical MCM-41 materials [42,43]. On the other hand, it is observed a slight increase of lattice parameter with the metal content, which could be consistent with some degree of metal incorporation into the framework. In addition, the high-angle XRD patterns of the samples with nominal Co loadings of 10 and 15 wt.% (Fig. 2) exhibit very small peaks (2θ=36.8°, 44.8°, 59.3° and 65.2°) characteristic of Co_3O_4 nano-particles, whose intensities increase with the higher loading level. It should be noted that the peaks characteristic of cobalt oxide are much attenuated in terms of intensity in relation to the major peak corresponding to MCM-41 structure. The mean crystallite sizes of oxide were estimated by the Scherrer equation using the most intense reflection of the phase. These values increased from around 6 to 7 $\pm$ 1 nm when the metal content increased up to ≈12 wt.%. Since the average diameter pore of MCM-41 is around 3 nm [44], these nano-oxides would be located on the external surface and in low amounts, judging by the low intensity of their diffraction peaks. Since it is known that some cations can form clusters in highly alkaline conditions [29], both Co oxide clusters and nano-particles could be formed by dehydration of cobalt hydroxide precipitated inside the mesopores or on the external surface of MCM-41. Therefore, besides these larger oxide crystals (detected by XRD), the presence of different metal species such as isolated cations, noncrystalline oxide clusters or smaller crystallites (non-detectable by XRD) linked or highly dispersed inside the channels cannot be discarded. Anyway, it is evident that the higher metal loading leads to higher amount, size and crystallinity of the impregnated oxides.

The N_2 adsorption–desorption isotherms for the samples are shown in Fig. 3. All the solids exhibit type IV isotherms, typical of well-defined mesoporous structure with an inflection at $P/P_0 \sim 0.1$–0.25 characteristic of capillary condensation inside the mesopores in the MCM-41 structure. The results obtained from the isotherms and other physicochemical parameters are collected in Table 1. All of the materials show high area values and pore volume, typical of MCM-41, although a decrease in these values is observed for the Co nominal loading of 15 wt.%. This behavior, consistent with the decreased structure ordering, can be also attributed to the increase in amount and size of the cobalt oxides formed both inside the channels and on the external surface. As it can be observed the pore wall thickness (t_w) is slightly increased with the Co nominal content increasing up to 10 wt.%, which could be giving account for the increased presence of different Co species finally dispersed inside the channels. The highest Co content would promote the growth of oxides particles on the external surface of the samples, causing high structure deterioration.

To get an insight into the coordination environment and the position of the cobalt in our materials, UV–vis DR spectra of the

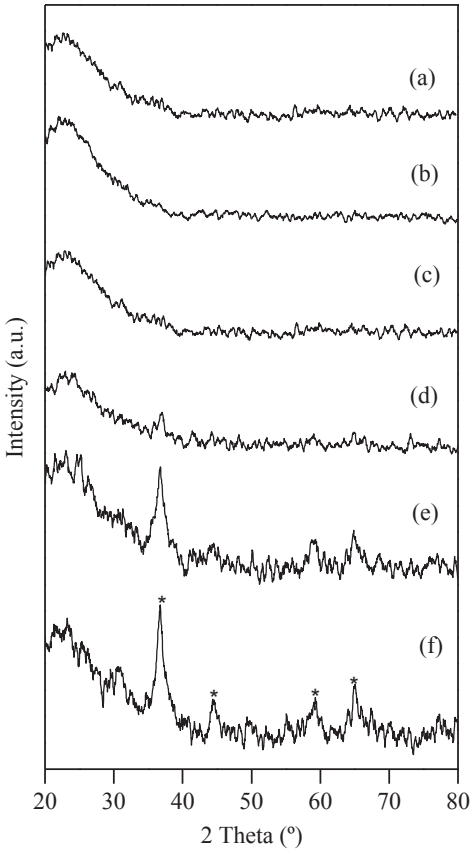

Fig. 2. High-angle XRD patterns of samples (a) MCM-41, (b) Co/M(1), (c) Co/M(2.5), (d) Co/M(5), (e) Co/M(10), (f) Co/M(15).

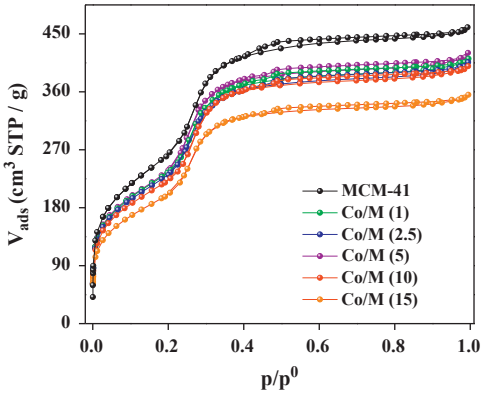

Fig. 3. Nitrogen adsorption–desorption isotherms of the synthesized samples.

Table 1
Structure properties and chemical composition of the synthesized samples.

Sample	Area[a] (m^2/g)	a_o (nm)	Dp[b] (nm)	t_w[c] (nm)	V_{TP} ($cm^3\,g^{-1}$)	Bulk Co (wt.%)[d]	Surface Co (wt.%)[e]
MCM-41	996	4.09	3.2	0.89	0.70	–	–
CoM(1)	888	4.18	3.0	1.18	0.63	0.80	0.77
CoM(2.5)	862	4.25	3.1	1.15	0.62	2.20	1.74
CoM(5)	862	4.27	3.0	1.27	0.64	4.35	3.54
CoM(10)	812	4.27	3.0	1.27	0.61	8.81	7.77
CoM(15)	730	4.03	3.2	0.83	0.54	11.90	9.88

[a] Determined by BET.
[b] Pore diameter determined by the BJH method.
[c] $t_w = a_0 - \mathrm{Dp}$.
[d] Determined method ICP.
[e] Determined by EPMA-EDS.

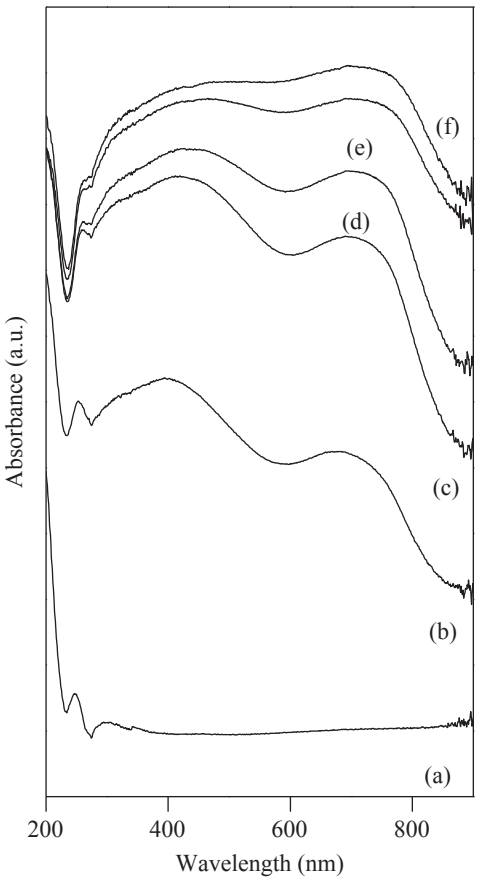

Fig. 4. UV–vis DR spectra of the samples (a) MCM-41, (b) Co/M(1), (c) Co/M(2.5), (d) Co/M(5), (e) Co/M(10), (f) Co/M(15).

calcined samples were recorded as presented in Fig. 4. A very broad absorption region between 200 and 860 nm, arising from the overlapping of absorptions corresponding to different Co species, can be observed. A band at around 260 nm, usually assigned to a charge transfer from the oxygen ligand to Co^{2+} ion in tetrahedral symmetry [27,28,31], is suggesting the presence of isolated Co^{2+} species into the framework. It is notable that this band gets better resolved for the sample with the lower Co loading. In this sense, Vralstad et al. [24] have recently reported that the precipitated hydroxide precursors can interact directly with silica species to be incorporated into the silica framework. On the other hand, absorptions between 300 and 400 nm could be originated from the characteristic electronic transitions of Co^{3+} in disordered tetrahedral environment, suggesting thus the oxidation of Co^{2+} to Co^{3+} after calcination [22–32]; meanwhile, absorptions between 400 and 600 nm can be assigned to octahedral Co^{2+} species, probably present in cobalt oxide clusters [29,30,45,46]. The absorption in this last range is clearly increased when the cobalt loading enhances, indicating that the octahedral Co species are increasing. Finally, the absorption region between 600 and 800 nm indicates the presence of cobalt oxide in the form of Co_3O_4 where Co^{2+} ions are in tetrahedral coordination and Co^{3+} ions are in octahedral positions [29,45–47]. This signal is also strongly increased with increasing the Co loading which is consistent with the presence of Co_3O_4 crystallites detected by XRD for the samples with the higher Co contents [Co/*M*(2.5–15)]. However, it is noteworthy that the samples with lower Co loadings also show this signal although Co_3O_4 crystallites were not detected by XRD. This suggests the low amount of Co_3O_4 on the samples or its very small crystallite size, not detectable by XRD. In addition, all of the as-synthesized samples were pink colored (corresponding to the hydrated $[Co(H_2O)_6]^{+2}$ octahedral complex) and after calcination color turns to brown. This color, typical of the Co_3O_4 oxide, becomes darker with increasing the Co loading, indicating the increased presence of this phase. In addition, Table 1 shows also the surface Co content determined by EPMA-EDS. Based on these data, it could be concluded that part of the cobalt in our samples is present as cobalt oxide clusters or Co_3O_4 nano-particles on the external surface of MCM-41, although the presence of the cobalt species confined inside the mesopores is increased with the Co loading increasing.

The reducibility of metal species has been a useful means for detecting the interactions between the metal and the support [48]. Since TPR is a bulky process, not all particles are exposed to hydrogen at the same time producing a dependence of the temperature maximum on the particle size. For bulky oxides is expected an increase in the temperature maximum with the particle size. However, metal oxides loaded or incorporated in inert supports may exhibit different reduction behaviors compared with the metal oxides unsupported. In this sense, the TPR profile of metal oxides supported on inert matrixes, such as MCM-41, are in general more complex than that of bulky metal oxides because there exists a wide range of variables including the particle size of the metal oxide and its interaction with the matrix. It is known that a decrease in the size of the metal oxide particles makes the reduction faster due to a higher surface/volume ratio although these smaller particles can interact more intensely with the support and slow down thus the reduction. Therefore, the reducibility of the materials would be the result of the competition of these two factors [49]. The TPR profiles of our samples with nominal Co loadings of 2.5–15 wt.% are presented in Fig. 5. Two reduction regions could be distinguished: one at low-temperature (LT) and one at high-temperature (HT) which can be ascribed to the reduction of metal oxide species with different dispersion and interaction with the support. A first doublet that appears in the temperature range 300–400 °C may be attributed to the Co_3O_4 particles not well dispersed and weekly interacting with the surface, which give rise to reduction at lower temperature [46,50,51]. It is well known that reduction of Co_3O_4 takes place in two steps; thus the first reduction peak corresponds to the process: $Co_3O_4 \rightarrow CoO$, while the second one corresponds to $CoO \rightarrow Co^0$ transition. On the other hand, the intense peak in the HT region can be attributed to Co^{3+} and Co^{2+} species, probably present in very small Co_3O_4 particles that are finely dispersed and interact strongly with the surface, resulting in its reduction at higher

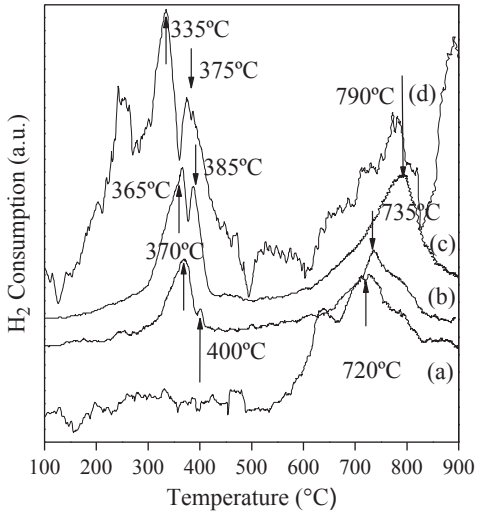

Fig. 5. TPR profiles of samples (a) Co/M(2.5), (b) Co/M(5), (c) Co/M(10) and (d) Co/M(15).

temperatures. For the Co/*M*(15) and Co/*M*(10) samples, the shift of the peaks, in the LT region, to lower temperatures (from 400/370 °C for Co/M(5) to 385/365 °C for Co/M(10) and to 375/335 °C for Co/M(15)) indicates a lower interaction of the Co_3O_4 particles (not well-dispersed and probably larger) with the support when the Co loading is increased. Meanwhile, the shift to higher temperatures (from 720 °C for Co/M(2.5) to 735 °C for Co/M (5) and to ~790 °C for the higher loaded samples) for the peak in the HT region would indicate a higher interaction of the smaller particles highly dispersed, when the Co loading is increased.

The magnetic curves at room temperature for the all of the samples are shown in Fig. 6. Given that the Co is the only possible source of a magnetic signal, the units of magnetization are emu per gram of cobalt. These materials present a diamagnetic contribution due to the silicon matrix [52], which is clearly observable for the sample with the lower metal loading (Fig. 6A). As expected, following the amount of cobalt loaded on the MCM-41 mesoporous supports, the samples show different magnetic behaviors depending on the dispersion and the size of the cobalt species. A paramagnetic contribution is noticeable from a cobalt loading of 2.20 wt.% (Co/M(2.5)), being observed susceptibility values around 6×10^{-5} emu/g Co Oe. This paramagnetic contribution could be mainly due to the isolated cobalt species as well as oxide clusters and Co_3O_4 nano-particles evidenced by XRD or UV–vis DR [53]. On the other hand, the superparamagnetic contribution can be assigned to the smaller oxides particles finely dispersed on MCM-41 with a size below the critical diameter. On the other hand subtracting the lineal contributions from the magnetic curves, the superparamagnetic and ferromagetic behaviors are more clearly evidenced, as it is shown in Fig. 6B. These curves were fitted and the obtained parameters are indicated in Table 2. The coercivity shows a decrease with the Co loading increase, suggesting an increase in the domain size [54]. The remanent magnetization and superparamagnetic magnetization show a similar behavior; the maximum observed for the loading of 2.20 wt.% (Co/M(2.5)) could be attributed to the small Co species finely dispersed on the matrix which then become larger for the higher Co loadings.

4. Conclusions

Co/MCM-41 nano-composites, with Co loadings between 0.8 and 12 wt.% were successfully prepared by the wet impregnation method. All the materials exhibited high specific surface, pore volume and good structural regularity, retaining the mesoporous structure even after the higher metal loading. However, certain decrease in the structural ordering, area and pore volume values was observed with increasing metal loading. The presence of different species was investigated through UV–vis DRS and TPR. Several metallic species such as isolated Co^{2+} species, oxide clusters and Co_3O_4 nano-particles were detected. The two last species increase in amount and size, when the Co loading is increased. Thus, larger Co_3O_4 nanocrystals, certainly located on the external surface could be also detected by XRD for the Co nominal loadings of 10 and 15 wt.%. Likewise, the confining of the cobalt species inside the mesopores could be achieved by increasing the cobalt loading. These nano-composites showed different magnetic properties depending on the dispersion and size of the cobalt species. Thus, a paramagnetic contribution, probably arising

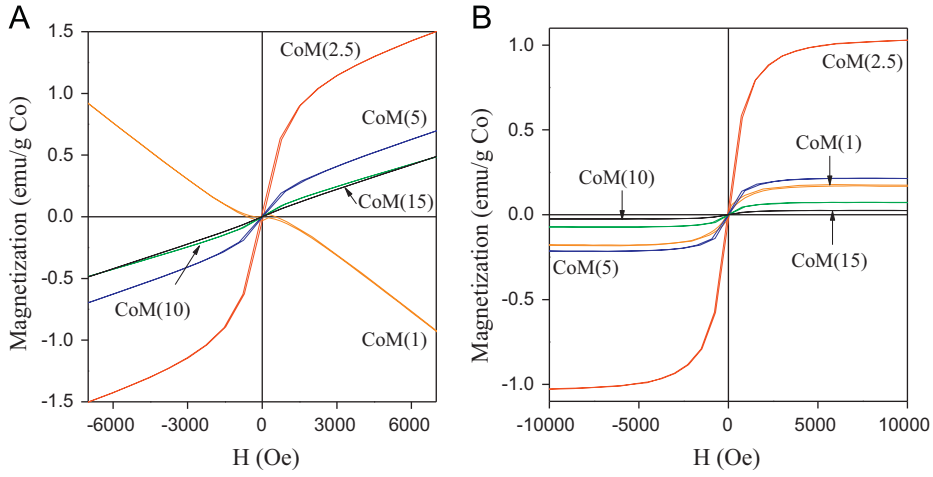

Fig. 6. Room temperature magnetic curves corresponding to the Co-modified samples.

Table 2
Magnetic parameters after fitting to data of Fig. 6B.

Sample	Hc[a] (Oe)	Mr[b] (emu/gCo)	M_{Sp}[c] (emu/gCo)	M_{fm}[d] (emu/gCo)	mμ[e] (μB)	H_m (Oe)[e]	X_{lineal}[f] (emu/gCo Oe)
CoM(1)	82	0.017	0.177	0.0057	11458	112.7	−1.5E−4
CoM(2.5)	47	0.03	1.065	0.002	12000	35	6.9E−5
CoM(5)	24.6	0.0044	0.091	0.134	12000	196	6.8E−5
CoM(10)	16.8	0.001	0.028	0.048	11316	158	5.9E−5
CoM(15)	11.5	0.00026	0.0027	O.024	12000	393	6.6E−5

[a] Hc: coercitive field.
[b] M_r: remanent moment.
[c] M_{Sp}: superparamagnetic effective saturation moment.
[d] M_{fm}: ferromagnetic effective saturation moment.
[e] mμ: mean magnetic moment of the superparamagnetic units.
[f] X_{lineal}: magnetic susceptibility.

from oxide clusters and nano-particles, becomes dominant for the samples highly loaded. Meanwhile, a superparamagnetic contribution enhanced for the lower loadings can be assigned to oxides of very small size finely dispersed.

Acknowledgments

The authors are grateful to CONICET, UTN-FRC and FaMAF-UNC for the financial support.

References

[1] T. Sen, A. Sebastianelli, I.J. Bruce, J. Am. Chem. Soc. 128 (2006) 7130–7131.
[2] J. Zhang, W. Sun, L. Bergman, J. Rosenholm, M. Lindén, G. Wu, H. Xu, H. Gu, Mater. Lett. 67 (2012) 379–382.
[3] T. Sathe, A. Agrawal, S. Nie, Anal. Chem. 78 (2006) 5627–5632.
[4] C. Kumar, J. Hormes, C. Leuschner, Nanofabrication Towards Biomedical Applications, Wiley-VCH, Weinheim, 2005.
[5] S. Mornet, S. Vasseur, F. Grasset, E.J. Duguet, J. Mater. Chem. 14 (2004) 2161–2175.
[6] J. Won, M. Kim, Y. Yi, Y.H. Kim, N. Jung, T.K. Kim, Science 309 (2005) 121–125.
[7] S. Laurent, S. Dutz, U. Häfeli, M. Mahmoudi, Adv. Colloid Interface Sci. 166 (2011) 8–23.
[8] H. Xua, Z. Aguilar, L. Yang, M. Kuang, H. Duan, Y. Xiong, H. Wei, A. Wang, Biomaterials 32 (2011) 9758–9765.
[9] M. Lakshmi Kantama, B.Purna Chandra Roa, R. Sudarshan Reddya, N. Sekhar, B. Sreedhar, B. Choudary, J. Mol. Catal. A 272 (2007) 1–5.
[10] R. Ryoo, S.H. Joo, S. Jun, J. Phys. Chem. B 103 (1999) 7743.
[11] S. Joo, S. Choi, I. Oh, J. Kwak, Z. Liu, R. Ryoo, Nature 412 (2001) 169–172.
[12] B. Lee, H.J. Im, H.M. Luo, E.W. Hagaman, S. Dai, Langmuir 21 (2005) 5372–5376.
[13] S. Wang, H.T. Li, Microporous Mesoporous Mater. 97 (2006) 21–26.
[14] M. Vallet-Regi, F. Balas, D. Arcos, Angew. Chem. Int. Ed. 46 (2007) 7548–7558.
[15] N. Botterhuis, Q. Sun, P.C.M.M. Magusin, R. Santen, N. Sommerdijk, Chem. Eur. J 12 (2006) 1448–1456.
[16] M. Vallet-Regi, Chem. Eur. J 12 (2006) 5934–5943.
[17] D. Yi, S. Lee, G. Papaefthymiou, J. Ying, Chem. Mater. 18 (2006) 614–619.
[18] J. Yu, H. Zhao, L. He, H. Yang, S. Ku, N. Yang, N. Xiao, J. Mater. Chem. 19 (2009) 1265–1270.
[19] E. Ruiz-Hernández, A. López-Noriega, D. Arcos, M. Vallet-Regí, Solid State Sci. 10 (2008) 421–426.
[20] L. Guo, J. Li, L. Zhang, J. Li, Y. Li, C. Yu, J. Shi, M. Ruan, J. Feng, J. Mater. Sci. 18 (2008) 2733–2738.
[21] S. Zhu, Z. Zhou, D. Zhang, C. Jin, Z. Li, Microporous Mesoporous Mater. 106 (2007) 56–61.
[22] S. Lim, C. Wang, Y. Yang, D. Ciuparu, L. Pfefferle, G. Haller, Catal. Today 123 (2007) 122–132.
[23] B. Viana de Sousa, M. Freire Rodrigues, L. Cano, M. Cagnoli, J. Bengoa, S. Marchetti, G. Pecchi, Catal. Today 172 (2011) 152–157.
[24] T. Vralstad, G. Oye, M. Stöcker, J. Sjöblom, Microporous Mesoporous Mater. 104 (2007) 10–17.
[25] A. Khodakov, V. Zholobenko, R. Bechara, D. Durand, Microporous Mesoporous Mater. 79 (2005) 29–39.
[26] V. Parvulescu, B. Su, Catal. Today 69 (2001) 315–322.
[27] S. Bhoware, S. Shylesh, K. Kamble, A. Singh, J. Mol. Catal. A 255 (2006) 123–130.
[28] M. Karthik, A. Tripathi, N. Gupta, A. Vinu, M. Hartmann, M. Palanichamy, V. Murugesan, Appl. Catal. A 268 (2004) 139–149.
[29] S. Bhoware, A. Singh, J. Mol. Catal. A 266 (2007) 118–130.
[30] S. Vetrivel, A. Pandurangan, J. Mol. Catal. A 227 (2005) 269–278.
[31] Z. Yuan, T. Chen, J. Wang, H. Li, Colloids Surf. A 179 (2001) 253–259.
[32] T. Somanathan, A. Pandurangan, D. Sathiyamoorthy, J. Mol. Catal. A 256 (2006) 193–199.
[33] M. Sato, S. Takada, S. Kohiki, T. Babasaki, H. Deguchi, M. Oku, M. Mitome, Appl. Phys. Lett. 77–78 (2000) 1194–1196.
[34] J. El Haskouri, S. Cabrera, C. Gómez-García, C. Guillem, J. Latorre, A. Beltrán, D. Beltrán, M. Dolores Marcos, P. Amorós, Chem. Mater. 16 (2004) 2805–2813.
[35] H. Emamian, A. Honarbakhsh-raouf, A. Ataie, A. Yourdkhani, J. Alloys Compd. 480 (2009) 681–683.
[36] A. Morey, N. Li, W. Hines, D. Perry, M. Jain, G. Haller, S. Suib., J. Appl. Phys. 110 (2011) 103904–103914.
[37] V. Elías, M. Crivello, E. Herrero, S. Casuscelli, G.A. Eimer, J. Non-Cryst. Solids 355 (2009) 1269–1273.
[38] A. Patterson, Phys. Rev. 56 (1939) 978–982.
[39] M. Stearns, Y. Cheng., J. Appl. Phys. 75 (1994) 6894–6898.
[40] P. Allia, M. Coisson, M. Knobel, P. Tiberto, F. Vinai., Phys. Rev. B. 60 (1999) 12207–12218.
[41] Y. Do, J. Kim, J. Park, S. Hong, C. Suh, G. Lee, Catal. Today 101 (2005) 299–305.
[42] C. Chanquía, K. Sapag, E. Rodriguez-Castellón, E. Herrero, G.A. Eimer, J. Phys. Chem. C 114 (2010) 1481–1490.
[43] G. Soller-Illia, C. Sanchez, B. Lebeau, J. Patarin, Chem. Rev. 102 (2002) 4093.
[44] V. Elías, E. Vaschetto, K. Sapag, M. Oliva, S. Casuscelli, G. Eimer, Catal. Today 172 (2011) 58–65.
[45] V. Elías, E. Vaschetto, K. Sapag, M. Crivello, S. Casuscelli, G. Eimer, Top. Catal. 54 (2011) 277–286.
[46] J. Smeets, Q. Meng, S. Corthals, H. Leeman, R. Schoonheydt, Appl. Catal. B 84 (2008) 505–513.
[47] I. Zacharaki, C. Kontoyannis, S. Boghosian, A. Lycourghiotis, Ch. Kordulis, Catal. Today 143 (2009) 38–44.
[48] B. Sun, E.P. Reddy, P.G. Smirniotis, Appl. Catal. B 57 (2005) 139–149.
[49] S. Rodrigues, S. Uma, I. Martyanov, K. Klabunde, J. Photochem. Photobiol. A 165 (2004) 51–58.
[50] T. Ataloglou, C. Fountzoula, K. Bourikas, J. Vakros, A. Lycourghiotis, C. Kordulis, Appl. Catal. A 288 (2005) 1–9.
[51] S. Todorova, V. Parvulescu, G. Kadinov, K. Tenchev, S. Somacescu, B. Su, Microporous Mesoporous Mater. 113 (2008) 22–30.
[52] L. Pierella, C. Saux, S. Caglieri, H. Bertorello, P. Bercoff, Appl. Catal. A 347 (2008) 55–61.
[53] W. Chen, C. Chen, L. Guo, J. Appl. Phys. 108 (2010) 073907–073912.
[54] B. Cullity, Introduction to Magnetic Materials, Addison Wesley, Reading, MA, 1972. (section 11.6).